Reducing bias in Y-90 PET images by enforcing non-negativity in projection space

Hongki Lim, Yuni K. Dewaraja, *Member, IEEE,* and Jeffrey A. Fessler, *Fellow, IEEE*

Abstract—Most existing PET image reconstruction methods impose a nonnegativity constraint in the image domain that is natural physically, but can lead to biased reconstructions. This bias is particularly problematic for Y-90 PET because of the low probability positron production and high random coincidence fraction. We propose a new PET reconstruction formulation that enforces nonnegativity of the projections instead of the voxel values. This formulation allows some negative voxel values thereby potentially reducing bias. To relax the non-negativity constraint embedded in the standard methods for PET reconstruction, we used an Alternating Direction Method of Multipliers (ADMM). Because choice of ADMM parameters can greatly influence convergence rate, we applied an automatic parameter selection method to improve the convergence speed. We investigated several variants differentiated by the base model and the constraint condition using lung to liver slices of XCAT phantom. We simulated low true coincidence count-rates with high random fractions corresponding to the typical values from patient imaging in Y-90 microsphere radioembolization. We compared our new methods with standard reconstruction algorithms. As the proposed algorithm iterates, the new method reduces the bias in cold spot while yielding lower noise than the standard method. The new model improves the quantification in all regions of interest when the methods achieve similar level of noise in the liver. The improvements with the new method are especially notable when simulating conditions corresponding to patients with lower activity administration (i.e., higher random fractions).

I. INTRODUCTION

Y-90 PET is complex because of the low probability positron production in the presence of increased singles events from bremsstrahlung photons and gammas from natural radioactivity in Lu-based crystals. Due to these attributes of Y-90, positive bias in cold regions and underestimation in regions of interest are reported in several Y-90 PET studies such as [2]. In this paper, we propose a method to relax the conventional image-domain nonnegativity constraint by instead imposing a nonnegativity constraint on the predicted sinogram means. To perform reconstruction that enforces this constraint, we adopt ADMM and derived several different models based on ADMM framework. The following subsection briefly reviews the typical problem formulation in emission tomography.

H. K. Lim is with the Department of Electrical Engineering and Computer Science, University of Michigan, Ann Arbor, MI 48109 USA (hongki@umich.edu).

Y. K. Dewaraja is with the Department of Radiology, University of Michigan, Ann Arbor, MI 48109 USA (yuni@med.umich.edu).

J. A. Fessler is with the Department of Electrical Engineering and Computer Science, University of Michigan, Ann Arbor, MI 48109 USA (fessler@umich.edu).

A. Emission Tomography

The goal in emission tomography is to find an emission distribution $\boldsymbol{x} = (x_1, ..., x_{n_p})$ [counts] from a realization $\boldsymbol{y} = (y_1, ..., y_{n_d})$ [counts] of the projection measurement vector $\boldsymbol{Y} = (Y_1, ..., Y_{n_d})$, where n_p is the number of voxels of unknown functional image and n_d is the number of rays. Emission measurement $\boldsymbol{Y}$ follows Poisson statistical model as follows:

$$Y_i \sim \text{Poisson}\{\bar{y}_i(\boldsymbol{x}_{\text{true}})\}, \quad i = 1, ..., n_d, \qquad (1)$$

where $\boldsymbol{x}_{\text{true}}$ is true unknown value that we want to estimate and $\bar{y}_i(\boldsymbol{x})$ [counts] is the measurement mean:

$$\bar{y}_i(\boldsymbol{x}) = \text{E}[Y_i] = \sum_{j=1}^{n_p} a_{ij} x_j + \bar{r}_i = [\boldsymbol{A}\boldsymbol{x}]_i + \bar{r}_i. \qquad (2)$$

The matrix $\boldsymbol{A}$ denotes the system model and $\bar{r}_i$ is the mean background events such as scatter and random coincidence for the ith ray. The maximum likelihood (ML) estimate $\hat{\boldsymbol{x}}$ of $\boldsymbol{x}_{\text{true}}$ minimizes the Poisson negative log-likelihood $f(\boldsymbol{x})$ between measurement and estimated measurement means:

$$f(\boldsymbol{x}) \stackrel{c}{=} \sum_{i=1}^{n_d} \bar{y}_i(\boldsymbol{x}) - y_i \log \bar{y}_i(\boldsymbol{x}). \qquad (3)$$

Here, $\stackrel{c}{=}$ indicates that we exclude constants independent of $\boldsymbol{x}$. The following formulation summarizes the conventional emission tomography problem:

$$\hat{\boldsymbol{x}} = \underset{\boldsymbol{x}}{\arg\min} f(\boldsymbol{x}) \qquad (4)$$

$$\text{subject to } \boldsymbol{x} \geq 0. \qquad (5)$$

The typical approach for solving this formulation is to find a surrogate function $Q(\boldsymbol{x})$ of the log-likelihood that is easier to monotonically decrease than $f(\boldsymbol{x})$.

II. PROPOSED FORMULATION

To loosen the nonnegativity constraint in hope of reducing the positive bias, we propose to allow negative values in image domain while keeping positivity in projection space. We propose the following formulation:

$$\hat{\boldsymbol{x}} = \underset{\boldsymbol{x}}{\arg\min} f(\boldsymbol{x}), \quad \text{subject to } \boldsymbol{A}\boldsymbol{x} + \bar{r} > 0. \qquad (6)$$

The constraint $\boldsymbol{A}\boldsymbol{x} + \bar{r} > 0$ is reasonable because likelihood function $f(\boldsymbol{x})$ includes $\log(\boldsymbol{A}\boldsymbol{x} + \bar{r})$ and the argument of a logarithm should be positive. We rewrite this optimization

problem in the following unconstrained composite formulation:

$$\hat{\boldsymbol{x}} = \operatorname*{argmin}_{\boldsymbol{x}\in\mathbb{R}^{n_p}} f(\boldsymbol{x}) + g(\boldsymbol{A}\boldsymbol{x} + \bar{\boldsymbol{r}}), \quad \text{where } g(\boldsymbol{v}) = \begin{cases} \infty, & \text{any } v_i < 0 \\ 0, & \text{all } v_i \geq 0 \end{cases} \tag{7}$$

for a vector argument $\boldsymbol{v} \in \mathbb{R}^{n_d}$. To perform this minimization, we introduce an auxiliary variable $\boldsymbol{z}$ leading to the following equality constrained optimization problem:

$$\hat{\boldsymbol{x}} = \operatorname*{argmin}_{\boldsymbol{x}\in\mathbb{R}^{n_p}} \min_{\boldsymbol{z}\in\mathbb{R}^{n_d}} f(\boldsymbol{x}) + g(\boldsymbol{z}), \quad \text{subject to } \boldsymbol{A}\boldsymbol{x} + \bar{\boldsymbol{r}} - \boldsymbol{z} = 0. \tag{8}$$

We form an augmented Lagrangian based on above problem formulation:

$$\Psi(\boldsymbol{x}, \boldsymbol{z}, \boldsymbol{\lambda}) = f(\boldsymbol{x}) + g(\boldsymbol{z}) + \boldsymbol{\lambda}^T(\boldsymbol{A}\boldsymbol{x} + \bar{\boldsymbol{r}} - \boldsymbol{z}) + \frac{\rho}{2}\|\boldsymbol{A}\boldsymbol{x} + \bar{\boldsymbol{r}} - \boldsymbol{z}\|_2^2, \tag{9}$$

where $\boldsymbol{\lambda}$ is a dual variable and $\rho > 0$ is called the penalty parameter. Letting $\boldsymbol{d} = \boldsymbol{A}\boldsymbol{x} + \bar{\boldsymbol{r}} - \boldsymbol{z}, \boldsymbol{u} = \frac{\boldsymbol{\lambda}}{\rho}$, we rewrite the augmented Lagrangian as the following equivalent expression:

$$\Psi(\boldsymbol{x}, \boldsymbol{z}, \boldsymbol{u}) = f(\boldsymbol{x}) + g(\boldsymbol{z}) + \frac{\rho}{2}\|\boldsymbol{A}\boldsymbol{x} + \bar{\boldsymbol{r}} - \boldsymbol{z} + \boldsymbol{u}\|_2^2 - \frac{\rho}{2}\|\boldsymbol{u}\|_2^2, \tag{10}$$

and finding the saddle point of (10) is equivalent to solving the problem (8):

$$\hat{\boldsymbol{x}} = \operatorname*{argmin}_{\boldsymbol{x}\in\mathbb{R}^{n_p}} \min_{\boldsymbol{z}\in\mathbb{R}^{n_d}} \max_{\boldsymbol{u}\in\mathbb{R}^{n_d}} \Psi(\boldsymbol{x}, \boldsymbol{z}, \boldsymbol{u}). \tag{11}$$

ADMM [1] approaches the saddle point of the augmented Lagrangian function by updating variables $\boldsymbol{x}, \boldsymbol{z}, \boldsymbol{u}$ in the following sequential way:

$$\boldsymbol{x}^{(n+1)} = \operatorname*{argmin}_{\boldsymbol{x}} \left(f(\boldsymbol{x}) + \frac{\rho}{2}\|\boldsymbol{A}\boldsymbol{x} + \bar{\boldsymbol{r}} - \boldsymbol{z}^{(n)} + \boldsymbol{u}^{(n)}\|_2^2 \right) \tag{12}$$

$$\boldsymbol{z}^{(n+1)} = \operatorname*{argmin}_{\boldsymbol{z}} \left(g(\boldsymbol{z}) + \frac{\rho}{2}\|\boldsymbol{A}\boldsymbol{x}^{(n+1)} + \bar{\boldsymbol{r}} - \boldsymbol{z} + \boldsymbol{u}^{(n)}\|_2^2 \right) \tag{13}$$

$$\boldsymbol{u}^{(n+1)} = \boldsymbol{u}^{(n)} + (\boldsymbol{A}\boldsymbol{x}^{(n+1)} + \bar{\boldsymbol{r}} - \boldsymbol{z}^{(n+1)}). \tag{14}$$

We initialize $\boldsymbol{z}^{(0)}$ and $\boldsymbol{u}^{(0)}$ as $\boldsymbol{A}\boldsymbol{x}^{(0)} + \bar{\boldsymbol{r}}$ and $\boldsymbol{0}$ respectively in the implementation. ADMM is an extension of the method of multipliers algorithm where (12), (13) can be viewed as a finding primal optimal points in a sequential fashion and (14) as finding a dual optimal point. Manually selecting parameter ρ of ADMM algorithm often leads to slow convergence. [8] proposed to adaptively tune the parameter to achieve faster convergence. We adopted this adaptive ADMM method in the implementation and investigated its efficacy.

III. VARIABLE UPDATES

The $\boldsymbol{z}$-update (13) is obvious because function $g(\boldsymbol{z})$ goes to infinity when it has negative value:

$$\boldsymbol{z}^{(n+1)} = [\boldsymbol{A}\boldsymbol{x}^{(n+1)} + \bar{\boldsymbol{r}} + \boldsymbol{u}^{(n)}]_+, \tag{15}$$

where $[.]_+$ enforces the nonnegativity. However, the $\boldsymbol{x}$-update (12) is nontrivial as there is no analytical solution. We approach this problem by iteratively updating $\boldsymbol{x}$ to minimize (descend) $\Psi(\boldsymbol{x}, \boldsymbol{z}^{(n)}, \boldsymbol{u}^{(n)})$. We rewrite the problem formulation as following:

$$\boldsymbol{x}^{(n+1)} = \operatorname*{argmin}_{\boldsymbol{x}} \left(f(\boldsymbol{x}) + \frac{\rho}{2}\|\boldsymbol{A}\boldsymbol{x} + \bar{\boldsymbol{r}} - \boldsymbol{z}^{(n)} + \boldsymbol{u}^{(n)}\|_2^2 \right)$$
$$= \operatorname*{argmin}_{\boldsymbol{x}} \left(f(\boldsymbol{x}) + h(\boldsymbol{x}) \right). \tag{16}$$

Because $h(\boldsymbol{x})$ is quadratic, it is straightforward to derive a separable quadratic surrogate function $Q_{h,j}$ for it [3]. Then, to update $\boldsymbol{x}$ we combine that surrogate with the separable surrogate function of $f(\boldsymbol{x})$.

A. EM-based x update

With EM-based surrogate for $f(x)$ [6], we find x_j minimizing $Q_{\text{EM},j} + Q_{h,j}$ by equating $\frac{\partial(Q_{\text{EM},j}(x_j;\boldsymbol{x}^{(n)})+Q_{h,j}(x_j;\boldsymbol{x}^{(n)}))}{\partial x_j}$ to zero. Zeroing the derivative and finding the root is as follows:

$$x_j^{(n+1)} = \operatorname{root}(\alpha, \beta, \nu), \tag{17}$$

where

$$\alpha = \rho \sum_{i=1}^{n_d} a_i a_{ij} \tag{18}$$

$$\beta = \frac{1}{2} \Big(\rho \sum_{i=1}^{n_d} a_{ij}([\boldsymbol{A}\boldsymbol{x}^{(n)}]_i + \bar{r}_i - z_i^{(n)} + u_i^{(n)}) + a_j \tag{19}$$

$$+ \rho \sum_{i=1}^{n_d} a_i a_{ij}(\gamma_j - x_j^{(n)}) \Big) \tag{20}$$

$$\nu = e_j^{(n)} x_j^{(n)} - \gamma_j \Big(\rho \sum_{i=1}^{n_d} a_{ij}([\boldsymbol{A}\boldsymbol{x}^{(n)}]_i + \bar{r}_i - z_i^{(n)} + u_i^{(n)}) \tag{21}$$

$$+ a_j - \rho \sum_{i=1}^{n_d} a_i a_{ij} x_j^{(n)} - e_j^{(n)} \Big). \tag{22}$$

The user-defined γ_j values can provide faster convergence [5] and one way to specify γ_j values is as follows:

$$\gamma_j = \min \frac{\bar{r}_i}{a_i}. \tag{23}$$

$\bar{y}_i^{(n)}$ is equivalent to $\bar{y}_i(x^{(n)})$. $e_j^{(n)}$ denotes $\sum_{i=1}^{n_d} a_{ij} \frac{y_i}{\bar{y}_i^{(n)}}$ and a_j is $\sum_{i=1}^{n_d} a_{ij}$. $\operatorname{root}(\alpha, \beta, \nu)$ returns the root of $0 = \alpha x^2 + 2\beta x - \nu$ for $\alpha > 0$. Using the numerically stable form:

$$\operatorname{root}(\alpha, \beta, \nu) = \begin{cases} \frac{\sqrt{\beta^2 + \alpha\nu} - \beta}{\alpha}, & \alpha > 0, \beta < 0 \\ \frac{\nu}{2\beta}, & \alpha = 0 \\ \frac{\nu}{\sqrt{\beta^2 + \alpha\nu} + \beta}, & \alpha > 0, \beta \geq 0. \end{cases} \tag{24}$$

B. SPS-based x update

With SPS-based surrogate for $f(x)$ [4], we update $\boldsymbol{x}$ using the Newton's method without any nonnegativity constraint:

$$x_j^{(n+1)} = x_j^{(n)} - \frac{\frac{\partial Q_{\text{SPS},j}(x_j;\boldsymbol{x}^{(n)})}{\partial x_j}\big|_{x_j=x_j^{(n)}} + \frac{\partial Q_{h,j}(x_j;\boldsymbol{x}^{(n)})}{\partial x_j}\big|_{x_j=x_j^{(n)}}}{\frac{\partial^2 Q_{\text{SPS},j}(x_j;\boldsymbol{x}^{(n)})}{\partial x_j^2} + \frac{\partial^2 Q_{h,j}(x_j;\boldsymbol{x}^{(n)})}{\partial x_j^2}} \tag{25}$$

$$= x_j^{(n)} - \frac{\sum_{i=1}^{n_d}(1 - \frac{y_i}{\bar{y}_i^{(n)}})a_{ij} + \rho \sum_{i=1}^{n_d} a_{ij}([\boldsymbol{A}\boldsymbol{x}^{(n)}]_i + \bar{r}_i - z_i^{(n)} + u_i^{(n)})}{\sum_{i=1}^{n_d} \check{c}_i^{(n)} a_{ij} a_i + \rho \sum_{i=1}^{n_d} a_{ij} a_i}. \tag{26}$$

$\check{c}_i^{(n)}$ denotes the optimal curvature [4]. Because optimal curvature $\check{c}_i^{(n)}$ is defined only for $[\boldsymbol{A}\boldsymbol{x}]_i \geq 0$, we use the curvature from Taylor expansion for the ith bin when $-\bar{r}_i < [\boldsymbol{A}\boldsymbol{x}]_i < 0$.
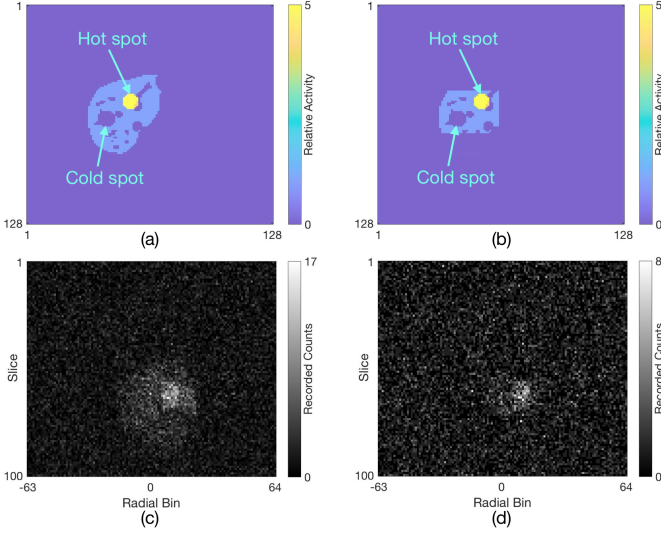
Fig. 1. True image and the corresponding projection: (a),(c) and (b),(d) are slices of true image and projection views at one angle simulating the conditions of patient A and B data respectively. Activity concentration ratio between healthy liver and hot spot (lesion) is 1:5 to simulate the typical uptake ratio.

IV. EXPERIMENTAL METHOD

A. Simulation

1) True image: We simulated extremely low-count scans, typical for Y-90 PET following radioembolization, with the extended cardiac-torso (XCAT) (Fig. 1). We set the image size to $128 \times 128 \times 100$ with a voxel size $4.0 \times 4.0 \times 4.0$ (mm^3) and chose 100 slices ranging from lung to liver. The activity concentration ratio between healthy liver and a 42mL lesion was 1:5 to simulate a typical uptake ratio. We also placed a 42mL zero valued cold spot in the liver. In one case activity was assigned to the entire liver, while in the other case only to part of the liver as lobar or segmental treatment is common. Activity assigned to the lungs simulated a lung shunt of 5%. The rest of the phantom is 'cold'.

2) Projection: Our experiment uses the framework of Michigan Image Reconstruction Toolbox (MIRT)[1]. We set the projection size to 128×100 with 168 projection angles and the detector width to 8mm when specifying the system model. For realistic simulation, we replicate the true and random counts observed in the patient imaging following radioembolization. Table I shows the low count conditions that we simulated corresponding to a relatively high Y-90 administration (Patient A) and a relatively low administration (Patient B) for patients treated at our clinic with glass microspheres. We use smaller area of liver (Fig. 1(b)) in the Patient B case because lower Y-90 administration and consequent lower true counts are usually induced by treatment of smaller region in the liver. Simulated projections are shown in Fig 1(c) and (d).

B. Evaluation metrics

We eroded each volume of interest (VOI) by 2 pixels to exclude resolution effects from the evaluation. We evaluated

[1]http://web.eecs.umich.edu/~fessler/code/index.html

TABLE I
ADMINISTERED ACTIVITY AND RANDOMS FRACTIONS FOR TWO PATIENTS TREATED AT OUR CLINIC WITH Y-90 RADIOEMBOLIZATION.

	Patient A	Patient B
Y-90 Injection(GBq)	3.9	0.9
True counts	675,498	96,890
Random counts	3,275,353	1,692,504
Total counts	3,950,851	1,789,394
Random Fraction* (%)	83	95

*Random Fraction = (True counts / Total counts)$\times$ 100

liver quantification by calculating activity recovery:

$$\text{Activity recovery in liver (\%)} = \frac{\text{Estimated mean counts}}{\text{True mean counts}} \times 100 \text{ \%} \quad (27)$$

$$= \frac{\frac{1}{M J_{\text{Liver}}} \sum_{m=1}^{M} \sum_{j \in \text{Liver}} \hat{\boldsymbol{x}}_m[j]}{\frac{1}{J_{\text{Liver}}} \sum_{j \in \text{Liver}} \boldsymbol{x}_{\text{true}}[j]} \times 100 \text{ \%}, \quad (28)$$

where M is the number of realizations and J_{Liver} is the number of voxels in the volume of liver. Estimated mean counts is calculated from the multiple realizations. We used 10 realizations in our experiment ($M = 10$). $\hat{\boldsymbol{x}}_m[j]$ indicates the jth voxel value at mth realization and $\boldsymbol{x}_{\text{true}}[j]$ denotes the jth voxel value of true counts.

Quantification in hot and cold spot (where true value of voxel is zero) are evaluated based on contrast recovery [2]:

$$\text{Contrast recovery in hot spot (\%)} = \frac{C_i/C_{\text{BKG}} - 1}{R - 1} \times 100 \text{ \%} \quad (29)$$

$$= \frac{\frac{\frac{1}{M J_{\text{Hotspot}}} \sum_{m=1}^{M} \sum_{j \in \text{Hotspot}} \hat{\boldsymbol{x}}_m[j]}{\frac{1}{J_{\text{Liver}}} \sum_{j \in \text{Liver}} \boldsymbol{x}_{\text{true}}[j]} - 1}{\frac{\frac{1}{J_{\text{Hotspot}}} \sum_{j \in \text{Hotspot}} \boldsymbol{x}_{\text{true}}[j]}{\frac{1}{J_{\text{Liver}}} \sum_{j \in \text{Liver}} \boldsymbol{x}_{\text{true}}[j]} - 1} \times 100 \text{ \%} \quad (30)$$

$$\text{Contrast recovery in cold spot (\%)} = (1 - \frac{C_i}{C_{\text{BKG}}}) \times 100 \text{ \%} \quad (31)$$

$$= \left(1 - \frac{\frac{1}{M J_{\text{Coldspot}}} \sum_{m=1}^{M} \sum_{j \in \text{Coldspot}} \hat{\boldsymbol{x}}_m[j]}{\frac{1}{J_{\text{Liver}}} \sum_{j \in \text{Liver}} \boldsymbol{x}_{\text{true}}[j]} \right) \times 100 \text{ \%}. \quad (32)$$

C_i is the mean counts for object i and C_{BKG} is mean background (eroded liver) counts. R is the true lesion-to-normal liver activity concentration ratio. We also study the counts bias the in field of view (FOV):

$$\text{FOV bias (\%)} = \frac{(\text{Total estimated counts} - \text{Total true counts})}{\text{Total true counts}} \times 100 \text{ \%} \quad (33)$$

$$= \frac{(\frac{1}{M} \sum_{m=1}^{M} \sum_{j=1}^{n_p} \hat{\boldsymbol{x}}_m[j] - \sum_{j=1}^{n_p} \boldsymbol{x}_{\text{true}}[j])}{\sum_{j=1}^{n_p} \boldsymbol{x}_{\text{true}}[j]} \times 100 \text{ \%}. \quad (34)$$

Lastly, we calculate the image ensemble noise across realizations averaged over the liver to evaluate the variability across realizations:

$$\text{Image ensemble noise (\%)} \quad (35)$$

$$= \frac{\sqrt{\frac{1}{J_{\text{Liver}}} \sum_{j \in \text{Liver}} \left(\frac{1}{M-1} \sum_{m=1}^{M} (\hat{\boldsymbol{x}}_m[j] - \frac{1}{M} \sum_{m'=1}^{M} \hat{\boldsymbol{x}}_{m'}[j])^2 \right)}}{\frac{1}{J_{\text{Liver}}} \sum_{j \in \text{Liver}} \boldsymbol{x}_{\text{true}}[j]} \times 100 \text{ \%}, \quad (36)$$

[2]http://www.nema.org/Standards/Pages/Performance-Measurements-of-Positron-Emission-Tomographs.aspx
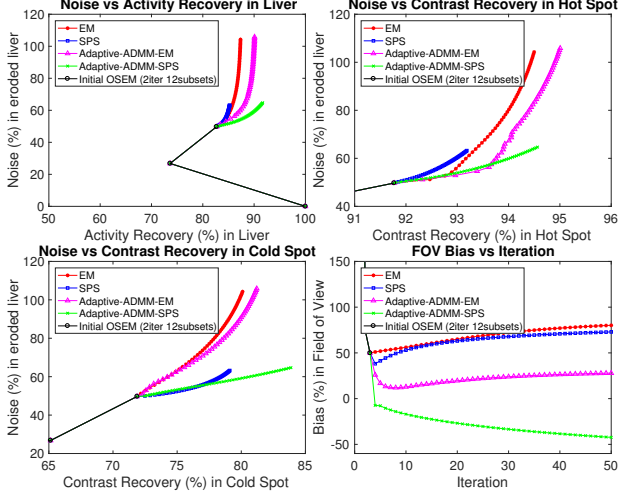
Fig. 2. Results from simulating Patient B conditions. Proposed algorithms (magenta, green) give higher contrast and better activity recovery compared to standard algorithms (EM, SPS).
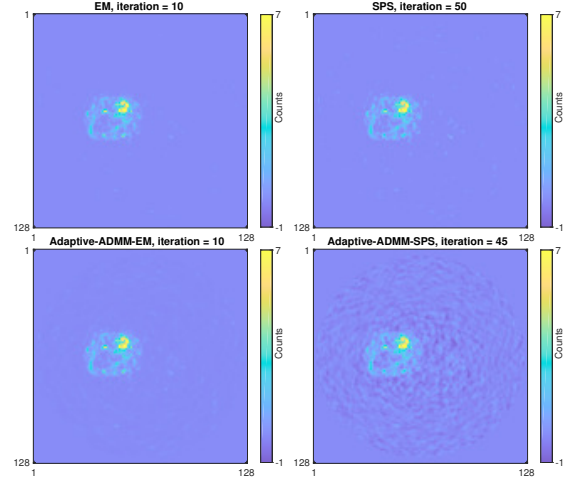

Fig. 3. Reconstructed images using EM, SPS and proposed algorithms (A-ADMM-EM, A-ADMM-SPS). Iteration number is chosen when each method achieve similar level of noise in liver. True image corresponds to Fig. 1(b).

TABLE II

EVALUATION METRICS COMPARISON WHEN ACHIEVING EQUIVALENT NOISE IN ERODED LIVER.

Condition	Algorithm	Iteration	ARL	CRH	CRC	FOVB	IEN
Patient A	EM	8	91.0	94.5	75.8	12.3	39.1
	SPS	50	91.7	94.3	81.6	14.5	38.7
	A-ADMM-EM	9	92.3	94.5	76.1	**2.6**	38.6
	A-ADMM-SPS	50	**94.1**	**94.6**	**83.8**	-7.5	38.7
Patient B	EM	10	85.8	93.4	75.2	58.8	63.9
	SPS	50	85.2	93.2	79.1	73.4	63.2
	A-ADMM-EM	10	88.1	93.9	75.2	**15.2**	63.7
	A-ADMM-SPS	45	**91.3**	**94.4**	**82.9**	-41.6	63.2

∗ARL: Activity Recovery in Liver, CRH: Contrast Recovery in Hot spot

CRC: Contrast Recovery in Cold spot, FOVB: FOV Bias

IEN: Image Ensemble Noise, A-ADMM: Adaptive-ADMM

V. RESULTS

We compared the proposed methods (Adaptive-ADMM-EM, Adaptive-ADMM-SPS) to the standard EM and SPS algorithms (1 subset). We use two iterations of OSEM algorithm with 12 subsets to initialize x for all algorithms because these are typical reconstruction parameters used for Y-90 in the clinic and we want to see how much each method can improve the quantification compared to the initial point.

Fig. 2 shows the results with plots showing how noise versus activity/contrast recovery in VOIs evolve with iterations. Fig. 2 also includes a plot of FOV bias versus iterations. Proposed algorithms achieve higher activity recovery in liver and contrast recovery in hot/cold spot compared to each base method (EM, SPS) when the noise in liver is similar to each other.

Table II summarizes the evaluation results at the iteration point when each method gives similar noise in liver. Proposed methods improve all the metrics compared to the standard methods. Improvement is notable in the Patient B case. In this lower activity administration case, when compared to standard SPS, A-ADMM-SPS improves activity recovery in liver by 6.1% and contrast recovery in hot spot and cold spot by 1.2%

and 3.8% respectively. A-ADMM-EM improves FOV bias by 43.6 % compared to standard EM. Fig. 3 visually compares the reconstructed images when each method achieves equivalent noise.

VI. CONCLUSION

This paper has presented a new PET reconstruction formulation with a relaxed nonnegativity constraint. The experimental results show that the proposed method reduces the bias in VOI when the true coincidence count-rate is low. Our proposed method is not limited to Y-90 PET but has application in other imaging situations with low true count rates and high random fractions such as the ion beam therapy [7].

REFERENCES

[1] S. Boyd, N. Parikh, E. Chu, B. Peleato, and J. Eckstein. Distributed optimization and statistical learning via the alternating direction method of multipliers. *Found. & Trends in Machine Learning*, 3(1):1–122, 2010.

[2] T. Carlier, K. P. Willowson, E. Fourkal, D. L. Bailey, M. Doss, and M. Conti. 90y-pet imaging: Exploring limitations and accuracy under conditions of low counts and high random fraction. *Medical physics*, 42(7):4295–4309, 2015.

[3] H. Erdogan and J. A. Fessler. Monotonic algorithms for transmission tomography. *IEEE Trans. Med. Imag.*, 18(9):801–14, Sept. 1999.

[4] J. A. Fessler and H. Erdogan. A paraboloidal surrogates algorithm for convergent penalized-likelihood emission image reconstruction. In *Proc. IEEE Nuc. Sci. Symp. Med. Im. Conf.*, volume 2, pages 1132–5, 1998.

[5] J. A. Fessler and A. O. Hero. Space-alternating generalized EM algorithms for penalized maximum-likelihood image reconstruction. Technical Report 286, Comm. and Sign. Proc. Lab., Dept. of EECS, Univ. of Michigan, Ann Arbor, MI, 48109-2122, Feb. 1994.

[6] J. A. Fessler and A. O. Hero. Penalized maximum-likelihood image reconstruction using space-alternating generalized EM algorithms. *IEEE Trans. Im. Proc.*, 4(10):1417–29, Oct. 1995.

[7] C. Kurz, J. Bauer, M. Conti, L. , L. Eriksson, and K. Parodi. Investigating the limits of PET/CT imaging at very low true count rates and high random fractions in ion-beam therapy monitoring. *Med. Phys.*, 42(7):3979–91, June 2015.

[8] Z. Xu, M. A. T. Figueiredo, and T. Goldstein. Adaptive ADMM with spectral penalty parameter selection, 2016. arxiv 1605.07246.